
Supervised Spike Agreement Dependent Plasticity for Fast Local Learning in Spiking Neural Networks

Gouri Lakshmi S¹ **Athira Chandrasekharan²** **Harshit Kumar¹** **Muhammed Sahad E²**
Bikas C Das² **Saptarshi Bej¹**

¹**School of Data Science, IISER Thiruvananthapuram, India**

²**School of Physics, IISER Thiruvananthapuram, India**

Correspondence: sbej7042@iisertvm.ac.in

Abstract

Spike-Timing-Dependent Plasticity (STDP) provides a biologically grounded learning rule for spiking neural networks (SNNs), but its reliance on precise spike timing and pairwise updates limits fast learning of weights. We introduce a supervised extension of Spike Agreement-Dependent Plasticity (SADP), which replaces pairwise spike-timing comparisons with population-level agreement metrics such as Cohen’s κ . The proposed learning rule preserves strict synaptic locality, admits linear-time complexity, and enables efficient supervised learning without backpropagation, surrogate gradients, or teacher forcing.

We integrate supervised SADP within hybrid CNN-SNN architectures, where convolutional encoders provide compact feature representations that are converted into Poisson spike trains for agreement-driven learning in the SNN. Extensive experiments on MNIST, Fashion-MNIST, CIFAR-10, and biomedical image classification tasks demonstrate competitive performance and fast convergence. Additional analyses show stable performance across broad hyperparameter ranges and compatibility with device-inspired synaptic update dynamics. Together, these results establish supervised SADP as a scalable, biologically grounded, and hardware-aligned learning paradigm for spiking neural networks.

1 Introduction

Spike-Timing-Dependent Plasticity (STDP) has long served as a foundational model for biologically plausible synaptic learning. Following the temporally asymmetric Hebbian principle, STDP strengthens synapses when a presynaptic spike precedes a postsynaptic spike (Long-Term Potentiation, LTP) and weakens them in the reverse order (Long-Term Depression, LTD) [3, 32]. Extensive experimental evidence supports this pairwise mechanism, and STDP has been widely employed to model learning in Spiking Neural Networks (SNNs) [4, 45]. In unsupervised settings, STDP has demonstrated effectiveness in extracting visual features from naturalistic stimuli, particularly when combined with competitive inhibition or convolutional architectures, achieving competitive performance on benchmarks such as MNIST, CIFAR-10, and FMNIST [34, 15, 25].

STDP is inherently a *local learning rule*, meaning that synaptic weight updates depend only on the activity of the *pre- and post-synaptic* neurons involved in the connection. Specifically, each synapse adjusts its efficacy based on the precise timing difference ($\Delta t = t_{\text{post}} - t_{\text{pre}}$) between local spike events, without requiring any global error signal, supervision, or knowledge of distant network states. This design reflects biological plausibility, as neurons in the brain cannot access global information but can sense local membrane potentials and spike timings.

The locality of STDP ensures scalability and energy efficiency, making it well-suited for neuromorphic hardware and decentralized computation. However, this same locality imposes key *limitations*: STDP alone cannot directly optimize global objectives such as classification accuracy or task-specific loss functions. It also struggles with credit assignment across multiple layers, temporal credit propagation, and long-range dependencies that require coordinated synaptic updates. As a result, while unsupervised STDP captures realistic neural plasticity, it often requires additional mechanisms, such as reward modulation or teacher forcing, to achieve complex goal-directed or supervised learning [24, 17].

Despite its success, classical STDP exhibits two primary limitations. First, it requires millisecond-scale spike timing precision, which is challenging to maintain in noisy or large-scale neural circuits [30, 31]. Second, its pairwise nature incurs quadratic computational complexity, as every pre-post spike pairing must be evaluated. These constraints hinder scalability and robustness in deep or real-time neuromorphic systems [48].

To overcome these challenges, population-level plasticity mechanisms have been proposed. Spike-Synchrony-Dependent Plasticity (SSDP) leverages coordinated activity among neuronal ensembles to guide synaptic adaptation, improving stability and reducing sensitivity to exact spike timing [48, 1]. Building on these insights, Spike Agreement-Dependent Plasticity (SADP) was recently introduced as a fast, local, and biologically inspired learning rule that generalizes classical STDP [2]. SADP quantifies alignment between pre- and post-synaptic spike trains over extended temporal windows using chance-corrected agreement metrics, such as Cohen’s κ , enabling linear-time synaptic updates and removing the need for strict causal ordering [2]. Empirical studies indicate that unsupervised SADP improves feature extraction efficiency and robustness while remaining compatible with diverse synaptic plasticity profiles [16, 9, 41, 2].

However, SADP has predominantly been restricted to unsupervised learning, limiting its applicability in tasks with explicit target signals [2]. In this work, we introduce a supervised SADP framework that integrates target-driven Hebbian updates at the output layer with κ -based agreement updates in hidden layers. The proposed method preserves the computational efficiency and biological plausibility of unsupervised SADP while enabling effective supervised training of multi-layer SNNs. Specifically, our approach leverages Poisson-encoded spike trains derived from raw or CNN-extracted features, applying agreement-based synaptic updates across SADP and SADP architectures with one and two hidden layers.

Contributions of this work are summarized as follows:

1. We propose a *supervised extension of Spike Agreement-Dependent Plasticity (SADP)* that enables fast, strictly local, and gradient-free learning in multi-layer spiking neural networks. The proposed Supervised SADP rule replaces precise spike-pair timing with population-level agreement metrics, achieving linear-time complexity while preserving biological plausibility.
2. We introduce a principled *CNN+Poisson hybrid encoding strategy* that allows agreement-based plasticity to scale from low-complexity grayscale datasets to visually rich color and biomedical images. By decoupling feature extraction from spike-based learning, the approach enables local synaptic adaptation in SNNs without backpropagating errors across layers.
3. We provide extensive empirical validation across standard vision benchmarks and biomedical imaging tasks, demonstrating that supervised SADP achieves competitive accuracy, faster convergence, and robust performance under limited hyperparameter tuning, while remaining compatible with device-inspired synaptic update dynamics.

The remainder of the paper is organized as follows. Section 2 reviews classical STDP and recent population-aware plasticity mechanisms, including SSDP. 3 details the supervised SADP model, learning rules, and multi-layer SNN architectures. Experimental details are described in 4. Empirical results and discussions are presented in 5.

2 Related Research

2.1 Classical Spike-Timing-Dependent Plasticity

Spike-Timing-Dependent Plasticity (STDP) is one of the most widely studied local learning rules in computational neuroscience. It formalizes Hebb’s principle by modifying synaptic weights according to the precise timing of pre- and post-synaptic spikes [32, 3]. Experimental studies have demonstrated robust Long-Term Potentiation (LTP) and Long-Term Depression (LTD) effects across multiple cortical regions [4, 45], which motivated extensive computational modeling in Spiking Neural Networks (SNNs).

In computational applications, STDP has been used for unsupervised feature extraction, particularly in visual domains. For instance, biologically plausible SNNs employing STDP can learn orientation-selective and edge-detecting filters from natural images [34, 15, 25]. However, STDP’s reliance on millisecond-scale spike precision and its quadratic computational complexity impose limitations on scalability, robustness, and real-time deployment [30, 31, 48].

2.2 Population and Synchrony-Dependent Plasticity

To overcome the limitations of classical STDP, research has explored higher-order and population-aware learning rules. One prominent approach is Spike-Synchrony-Dependent Plasticity (SSDP), which modulates synaptic updates based on the degree of coordinated spiking among neuron ensembles [8, 48]. SSDP reduces sensitivity to exact spike timing by leveraging synchronous activity patterns, which are believed to play a critical role in biological learning. By integrating ensemble-level correlations, SSDP improves the stability of learning and enhances robustness to noise while preserving the locality of synaptic updates. Several studies have demonstrated that synchrony-dependent rules can accelerate feature learning and facilitate pattern recognition in SNNs, particularly under noisy conditions [1].

2.3 Spike Agreement-Dependent Plasticity (SADP)

Building upon these insights, Spike Agreement-Dependent Plasticity (SADP) was recently proposed as a fast, local, and biologically inspired learning rule [48, 1]. Unlike STDP and SSDP, SADP measures the statistical agreement between pre- and post-synaptic spike trains over extended temporal windows using chance-corrected metrics such as Cohen’s κ . SADP eliminates the need for precise spike-pair evaluation, reducing computational complexity to linear time and making it highly compatible with hardware implementations. Empirical studies have shown that unsupervised SADP improves the speed and stability of learning in SNNs, enabling efficient feature extraction and robust pattern recognition across multiple encoding schemes and network configurations [16, 9, 41].

2.4 Reward-Based and Reinforcement-Driven Plasticity

In addition to unsupervised approaches, reward-modulated plasticity has emerged as a powerful mechanism for task-driven learning in SNNs. These rules extend Hebbian or STDP-based updates by incorporating a global or delayed reward signal that modulates synaptic changes [46, 38]. The three-factor learning rule is one of the most prominent frameworks, where synaptic updates depend on presynaptic activity, postsynaptic firing, and an external modulatory signal representing reward or error [36]. This paradigm bridges the gap between biologically plausible mechanisms and reinforcement learning principles, enabling SNNs to solve goal-directed tasks such as decision-making and motor control. However, reward-based schemes often require extensive exploration and exhibit slower convergence for high-dimensional pattern recognition problems.

2.5 Teacher-Forcing and Target-Driven Learning in SNNs

Another line of supervised SNN research employs teacher-forcing or direct target-driven learning. In these methods, the postsynaptic neurons receive external currents or surrogate targets that drive their firing activity to match desired output spike trains [13, 10]. This allows supervised training without explicit gradient computation, offering a biologically interpretable alternative to backpropagation through time. Despite their effectiveness, teacher-forcing approaches can introduce artificial supervision signals that reduce biological plausibility and are often sensitive to the duration or strength

Table 1: Reported classification accuracy (%) of SNN learning rules on standard vision benchmarks, extracted from Tian et al. [48]. Results are reproduced for reference only.

| Dataset | Learning Rule | Accuracy (%) |
|---------------|------------------------------|--------------|
| Fashion-MNIST | Sym-STDP [21] | 85.3 |
| | GLSNN [51] | 89.1 |
| | STB-STDP | 87.0 |
| | R-STDP | 83.26 |
| | SSTDP | 85.16 |
| | S2-STDP | 85.88 |
| N-MNIST | STDP | 98.74 |
| | Synaptic Kernel Inverse [11] | 92.87 |
| | BP-SNN | 92.7 |
| | STDP+CDNA-SNN [44] | 98.43 |
| CIFAR-10 | STB-STDP | 32.95 |
| | R-STDP | 51.74 |
| | S2-STDP | 61.80 |
| | SSTDP | 60.80 |
| | NCG-S2-STDP [19] | 66.41 |

of the teaching input [12]. Consequently, recent research has sought mechanisms that integrate the local, spike-based nature of Hebbian learning with global supervision, without relying on explicit teacher currents.

Recent-most benchmarks Recent work has demonstrated that population-level plasticity mechanisms can significantly outperform classical pairwise STDP in complex learning tasks. In particular, Tian et al. [48] showed that synchrony-based learning rules (SSDP, S2-STDP) achieve substantially higher accuracy than pairwise STDP variants across datasets such as Fashion-MNIST, CIFAR-10, and SHD, while maintaining local learning dynamics. These results provide strong evidence that ensemble-level spike statistics offer a more scalable substrate for learning than precise spike-timing relationships.

Supervised SADP follows this same direction by replacing spike-pair evaluation with agreement-based statistics following the unsupervised SADP version proposed by Bej *et al.* [2], but differs in two critical aspects: (i) agreement is quantified using chance-corrected metrics such as Cohen’s κ , providing robustness to firing-rate bias, and (ii) supervision is incorporated through local Hebbian updates at the output layer without teacher forcing or reward modulation. As a result, SADP retains the efficiency benefits of population-based plasticity while enabling task-driven learning in multilayer SNNs.

3 Supervised Spike Agreement-Dependent Plasticity

3.1 Input Representation and Encoding

3.1.1 Poisson Spike Encoding

Normalized input features are converted into stochastic spike trains of length T using independent Bernoulli sampling. For sample b , feature i , and timestep t ,

$$S_{\text{in}}^{(b)}(t, i) \sim \text{Bernoulli}\left(x_i^{(b)}\right).$$

This produces a binary spike tensor

$$\mathbf{S}_{\text{in}}^{(b)} \in \{0, 1\}^{T \times N_{\text{in}}},$$

which serves as the input to the spiking neural network.

Remark: Encoding for complex images. For low-complexity grayscale datasets such as MNIST and Fashion-MNIST, class-discriminative information is strongly correlated with pixel intensity patterns. In these cases, brightness-driven Poisson encoding provides sufficiently heterogeneous spike statistics for downstream spiking neurons to self-organize using local plasticity rules. As a result, meaningful feature selectivity can emerge even when raw pixel intensities are directly converted into spike trains.

However, this assumption does not hold for visually complex datasets such as CIFAR-10 or biomedical color images. In such cases, objects belonging to different classes often share similar brightness distributions, while discriminative cues arise from higher-order spatial, textural, and chromatic relationships. A purely brightness-based Poisson encoder therefore produces nearly homogeneous spike statistics across samples, depriving the spiking network of the structured variability required for effective specialization. Under these conditions, agreement-based plasticity converges to trivial or weakly discriminative representations.

The convolutional encoder addresses this limitation by transforming raw sensory input into a compact set of semantically meaningful feature activations prior to spike generation. These features, when converted into Poisson spike trains, provide the diversity and structure necessary for spike agreement-dependent plasticity to reinforce class-relevant neuronal assemblies. In this sense, the CNN acts as a sensory front-end that extracts informative signals, while the spiking network performs local, biologically inspired learning on temporally encoded representations.

Importantly, the introduction of a pretrained CNN does not alter the locality of learning within the spiking network. All synaptic updates in the SNN remain strictly local, depending only on pre- and post-synaptic spike activity and neuron-specific agreement signals. The CNN parameters are frozen during spiking training and do not receive feedback from the SNN, preserving the local and hardware-compatible nature of the learning dynamics. This separation allows the hybrid CNN-SNN architecture to combine the representational power of deep feature extraction with the interpretability and locality of spike-based plasticity.

3.1.2 CNN Feature Extraction for Complex Images

For visually complex datasets such as CIFAR-10 and biomedical images, a compact convolutional encoder is used to extract discriminative spatial features prior to spike generation. The encoder consists of three convolutional layers with ReLU activations, interleaved with max-pooling, followed by global average pooling and a dense projection layer. The encoder outputs a feature vector

$$\mathbf{x}^{(b)} \in [0, 1]^{N_{\text{in}}}.$$

The CNN encoder is pretrained using cross-entropy loss on class labels and remains frozen during spiking network training. For simpler grayscale datasets such as MNIST and Fashion-MNIST, the encoder is omitted and normalized pixel intensities are directly used as input features. All features are min-max normalized to the range $[0, 1]$.

3.2 Spiking Neuron Dynamics

All neurons are modeled as leaky integrate-and-fire (LIF) units. For layer l , sample b , and timestep t , the membrane potential evolves as

$$\mathbf{V}_l^{(b)}(t) = \lambda \mathbf{V}_l^{(b)}(t-1) + \mathbf{I}_l^{(b)}(t),$$

where $\lambda \in (0, 1)$ is the leak factor.

A neuron emits a spike when its membrane potential exceeds a fixed threshold:

$$\mathbf{s}_l^{(b)}(t) = \mathbb{I}(\mathbf{V}_l^{(b)}(t) > \theta_l).$$

After firing, the membrane potential is reset to zero:

$$\mathbf{V}_l^{(b)}(t) \leftarrow \mathbf{V}_l^{(b)}(t)(1 - \mathbf{s}_l^{(b)}(t)).$$

3.3 Network Architectures

3.3.1 1SADP Architecture with 1 Hidden Layer

The single-hidden-layer architecture consists of weight matrices

$$W_1 \in \mathbb{R}^{N_{\text{in}} \times N_h}, \quad W_2 \in \mathbb{R}^{N_h \times N_{\text{out}}}.$$

Input currents are computed as

$$\mathbf{I}_1^{(b)}(t) = \mathbf{S}_{\text{in}}^{(b)}(t) W_1, \quad \mathbf{I}_2^{(b)}(t) = \mathbf{s}_1^{(b)}(t) W_2.$$

We will refer to this architecture as 1SADP throughout the paper.

3.3.2 SADP Architecture with 2 Hidden Layers

The two-hidden-layer extension introduces an additional weight matrix

$$W_{1,2} \in \mathbb{R}^{N_h \times N_h}.$$

The corresponding currents are

$$\mathbf{I}_2^{(b)}(t) = \mathbf{s}_1^{(b)}(t) W_{1,2}, \quad \mathbf{I}_3^{(b)}(t) = \mathbf{s}_2^{(b)}(t) W_2.$$

No recurrent connections or teacher-forcing currents are used. We will refer to this architecture as 2SADP throughout the paper.

3.4 Output Decoding

After simulating T timesteps, output spike counts are accumulated as

$$\mathbf{C}^{(b)} = \sum_{t=1}^T \mathbf{s}_{\text{out}}^{(b)}(t).$$

The predicted class is

$$\hat{y}^{(b)} = \arg \max_k C_k^{(b)}.$$

3.5 Learning Rules

Importantly, the supervision signal does not propagate across layers; it is applied only at the output synapses, preserving strict locality of plasticity. Therefore, all learning rules are local, spike-driven, and gradient-free. Weight updates are applied once per mini-batch.

3.5.1 Supervised Hebbian Learning at the Output Layer

Let $\mathbf{y}^{(b)} \in \{0, 1\}^{N_{\text{out}}}$ denote the one-hot class label. The instantaneous output error signal is defined as

$$\mathbf{E}^{(b)}(t) = \mathbf{y}^{(b)} - \mathbf{s}_{\text{out}}^{(b)}(t).$$

The output-layer weight update is

$$\Delta W_2 = \frac{1}{B} \sum_{b=1}^B \sum_{t=1}^T (\mathbf{s}_{\text{pre}}^{(b)}(t))^{\top} \mathbf{E}^{(b)}(t),$$

where \mathbf{s}_{pre} denotes the spike activity of the final hidden layer.

Weights are updated using learning rate η_{out} , multiplicative decay ρ , and clipping:

$$W_2 \leftarrow \text{clip}(\rho W_2 + \eta_{\text{out}} \Delta W_2, [-W_{\text{max}}, W_{\text{max}}]).$$

3.5.2 Spike Agreement–Dependent Plasticity (SADP)

Hidden layers are trained using spike agreement–dependent plasticity, which reinforces neurons whose spike trains agree with the correct-class output neuron beyond chance.

Let

$$s_o^{*(b)}(t) = s_{\text{out}, y^{(b)}}^{(b)}(t)$$

denote the spike train of the correct-class output neuron.

For hidden neuron j , the observed agreement is

$$P_{o,j}^{(b)} = \frac{1}{T} \sum_{t=1}^T \mathbb{I}(s_{h,j}^{(b)}(t) = s_o^{*(b)}(t)).$$

The marginal firing probabilities are

$$p_{h,j}^{(b)} = \frac{1}{T} \sum_t s_{h,j}^{(b)}(t), \quad p_o^{(b)} = \frac{1}{T} \sum_t s_o^{*(b)}(t),$$

and the expected agreement by chance is

$$P_{e,j}^{(b)} = p_{h,j}^{(b)} p_o^{(b)} + (1 - p_{h,j}^{(b)}) (1 - p_o^{(b)}).$$

Cohen’s kappa coefficient is computed as

$$\kappa_j^{(b)} = \frac{P_{o,j}^{(b)} - P_{e,j}^{(b)}}{1 - P_{e,j}^{(b)} + \varepsilon}.$$

3.5.3 Input-to-Hidden Weight Update

Input-to-hidden synapses are updated using rate-based Hebbian correlations modulated by κ :

$$\Delta W_1 = \frac{1}{B} \sum_{b=1}^B (\mathbf{x}^{(b)})^\top \boldsymbol{\kappa}^{(b)}.$$

Weights are updated with decay and column-wise normalization:

$$W_1 \leftarrow \rho W_1 + \eta_{\text{in}} \Delta W_1, \quad W_{1,:,j} \leftarrow \frac{W_{1,:,j}}{\|W_{1,:,j}\|_2 + \varepsilon}.$$

3.5.4 Extension to 2SADP

For the second hidden layer, SADP is applied hierarchically using mean firing rates:

$$\Delta W_{1,2} = \frac{1}{B} \sum_{b=1}^B (\bar{\mathbf{s}}_1^{(b)})^\top \boldsymbol{\kappa}_2^{(b)}, \quad \bar{\mathbf{s}}_1^{(b)} = \frac{1}{T} \sum_t \mathbf{s}_1^{(b)}(t).$$

Only the output layer receives direct supervision; all preceding layers self-organize through spike agreement. Supervision enters the network exclusively through local mechanisms: (i) error-modulated Hebbian learning at the output layer, and (ii) agreement-based reinforcement using Cohen’s κ in hidden layers. No backpropagation, surrogate gradients, or teacher forcing are employed.

Computational Complexity. The computational complexity of supervised SADP scales linearly with the number of synapses and timesteps. Agreement metrics such as Cohen’s κ are computed using aggregate spike statistics over temporal windows, avoiding explicit enumeration of pre-post spike pairs. As a result, the hidden-layer plasticity updates scale as $\mathcal{O}(T)$ per neuron, in contrast to classical STDP, which incurs $\mathcal{O}(T^2)$ complexity due to pairwise spike-timing evaluations. Output-layer updates are similarly linear in the number of spikes. This linear-time behavior, combined with local memory access patterns, makes supervised SADP well suited for large-scale simulations and neuromorphic hardware implementations.

4 Experiments

4.1 Primary Benchmarking Experiments

The proposed supervised activity-dependent plasticity (SADP) framework was first evaluated across three benchmark image classification datasets: MNIST, Fashion-MNIST, and CIFAR-10. Each dataset was normalized to the range $[0, 1]$ and, where applicable, reshaped to include a channel dimension. We perform experiments on more datasets which is detailed later.

4.1.1 Datasets for Primary Benchmarking

To evaluate the proposed Supervised SADP algorithm, we test its performance first on three benchmark image classification datasets: **MNIST**, **Fashion-MNIST (FMNIST)**, and **CIFAR-10**.

MNIST. The MNIST dataset consists of 70,000 grayscale images of handwritten digits (0–9), each of size 28×28 . It is divided into 60,000 training and 10,000 testing samples. Since each digit’s category correlates strongly with pixel intensity patterns, MNIST serves as a baseline for evaluating spiking encoders on low-complexity, intensity-driven data.

Fashion-MNIST. Fashion-MNIST contains 70,000 grayscale images of size 28×28 , distributed across ten clothing categories such as *T-shirt*, *Trouser*, *Pullover*, and *Sandal*. It provides a more challenging alternative to MNIST by introducing complex textures and shapes while maintaining the same input dimensionality. This dataset tests whether the proposed Poisson encoding and Supervised SADP weight updates generalize beyond simple digit-like structures.

CIFAR-10. The CIFAR-10 dataset comprises 60,000 color images of size $32 \times 32 \times 3$, spanning ten object classes including *airplane*, *automobile*, *bird*, *cat*, *deer*, *dog*, *frog*, *horse*, *ship*, and *truck*. Unlike MNIST and Fashion-MNIST, CIFAR-10 involves rich visual features such as edges, textures, and color contrasts. These cues are not directly accessible through pixel intensity, making it necessary to employ a CNN-based feature extractor prior to Poisson encoding. This justifies the inclusion of the CNN encoder described in Section 3.1.2.

4.1.2 Encoding Types and Tested Architectures

Two types of input encodings were examined:

- **Poisson-only encoding:** Raw pixel intensities were converted into stochastic spike trains using Poisson sampling.
- **CNN+Poisson encoding:** A compact convolutional encoder (three convolutional layers followed by a global average pooling and dense projection layer) was pretrained using cross-entropy loss for up to 50 epochs. The resulting features were normalized and converted to Poisson spike trains for spiking neural network (SNN) processing. For CNN+Poisson encoding, the convolutional encoder outputs a 256-dimensional feature vector, which is subsequently normalized and converted into Poisson spike trains. This feature dimensionality was fixed across all datasets unless stated otherwise.

We implemented the 1SADP and 2SADP version, that is SNN neural networks with one and two hidden layers for final classification respectively.

4.1.3 Model Parameters

We performed a parameter sensitivity analysis for proposed architecture and the results are reported in Appendix A. However, we assumed standard well accepted parameter values for our main benchmarking experiments. This ensures that the learning is robust and not too much of parameter tuning is necessary in dataset specific cases to achieve standard results.

Each spiking model was trained for 50 epochs with mini-batch size of 128. Synaptic updates were driven by a local Hebbian rule for the output weights W_2 , and by the kappa-based SADP rule for the first hidden layer weights W_1 . For W_2 , the update is proportional to the correlation between hidden-layer spikes and output errors. For W_1 , Cohen’s kappa quantifies the statistical agreement between

hidden-layer spikes and target spike trains, modulating the weight updates. A small decay factor (0.9995) was applied per iteration to maintain stability, W_1 was normalized, and W_2 was clipped to prevent runaway growth.

Two temporal resolutions ($T = 25$ and $T = 100$ timesteps) were used to study the effect of spike duration on learning dynamics. Learning rates were set to $\eta_{\text{out}} = 5 \times 10^{-4}$ for supervised Hebbian updates and $\eta_{\text{in}} = 2 \times 10^{-4}$ for SADP updates. Model evaluation metrics included accuracy, macro-averaged F1-score computed over the test set and Runtime per Epoch.

4.2 Evaluation on Biomedical Image Datasets

To evaluate the generalization capability of the proposed classification framework beyond standard vision benchmarks, we conducted experiments on two bio-inspired medical imaging datasets: the LC25000 histopathology dataset [7] and a Brain MRI Tumor dataset [39]. These datasets differ significantly in color composition, spatial complexity, and diagnostic cues, providing a stringent test of the adaptability of the proposed learning rule. Another reason to choose these two datasets are that both histopathological and MRI images are widely explored modalities in computer vision research in the medical domain.

LC25000. The LC25000 dataset consists of 25,000 color histopathological images of size 768×768 , distributed evenly across five tissue classes: lung benign, lung adenocarcinoma, lung squamous cell carcinoma, colon adenocarcinoma, and colon benign tissue. The dataset was constructed from 1,250 validated pathology images and expanded through extensive data augmentation using the Augmentor framework. For experimental evaluation, the dataset was partitioned into two subsets: (i) Colon Histopathology, a binary classification task comprising colon benign and colon adenocarcinoma images, and (ii) Lung Histopathology, a three-class classification task involving lung benign tissue, adenocarcinoma, and squamous cell carcinoma.

Brain MRI Tumor. The Brain MRI Tumor dataset contains grayscale magnetic resonance images belonging to two categories: tumor and normal. All images were preprocessed through a curated pipeline that included removal of duplicates, correction of mislabeled samples, resizing to 224×224 , and data augmentation techniques such as histogram equalization, brightness adjustment, rotation, flipping, and noise injection. This dataset serves as a representative benchmark for grayscale medical image classification under limited contrast variability.

All datasets were evaluated using both Poisson-only and CNN+Poisson encoding schemes, across 1SADP and 2SADP architectures and temporal resolutions of $T = 25$ and $T = 100$ timesteps.

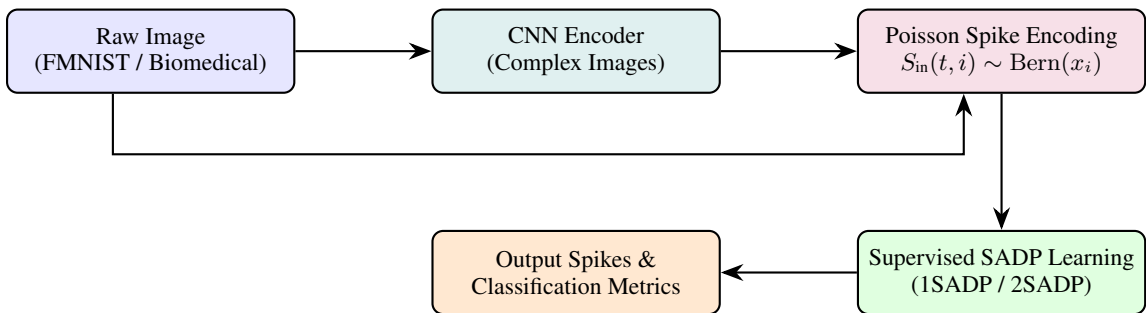


Figure 1: Pastel-colored experimental workflow: Poisson or CNN+Poisson encoding feeds into evaluation, which then connects to supervised SADP learning.

5 Results and Discussion

5.1 Results of the Primary Benchmarking Experiments

Effect of Encoding Schemes Table 2 presents the results obtained using the Poisson-only encoder. The Poisson encoder generates spikes proportional to pixel brightness, thereby effectively capturing temporal variations in simple grayscale images. Consequently, MNIST and FMNIST comprising

Table 2: Performance of Poisson-only encoding across datasets, architectures, and temporal resolutions.

| Dataset | Arch. | T | Accuracy | F1-score | Time/Epoch (s) |
|----------|-------|-----|----------|----------|----------------|
| CIFAR-10 | 1SADP | 25 | 0.2359 | 0.1741 | 239.88 |
| CIFAR-10 | 1SADP | 100 | 0.2359 | 0.1741 | 242.80 |
| CIFAR-10 | 2SADP | 25 | 0.2204 | 0.1532 | 364.36 |
| CIFAR-10 | 2SADP | 100 | 0.2204 | 0.1532 | 238.16 |
| FMNIST | 1SADP | 25 | 0.7585 | 0.7422 | 81.62 |
| FMNIST | 1SADP | 100 | 0.7585 | 0.7422 | 81.09 |
| FMNIST | 2SADP | 25 | 0.7600 | 0.7429 | 84.46 |
| FMNIST | 2SADP | 100 | 0.7600 | 0.7429 | 109.17 |
| MNIST | 1SADP | 25 | 0.8792 | 0.8759 | 109.60 |
| MNIST | 1SADP | 100 | 0.8792 | 0.8759 | 108.81 |
| MNIST | 2SADP | 25 | 0.8800 | 0.8787 | 82.99 |
| MNIST | 2SADP | 100 | 0.8800 | 0.8787 | 84.33 |

Table 3: Performance of CNN+Poisson Encoding across datasets, architectures, and temporal resolutions.

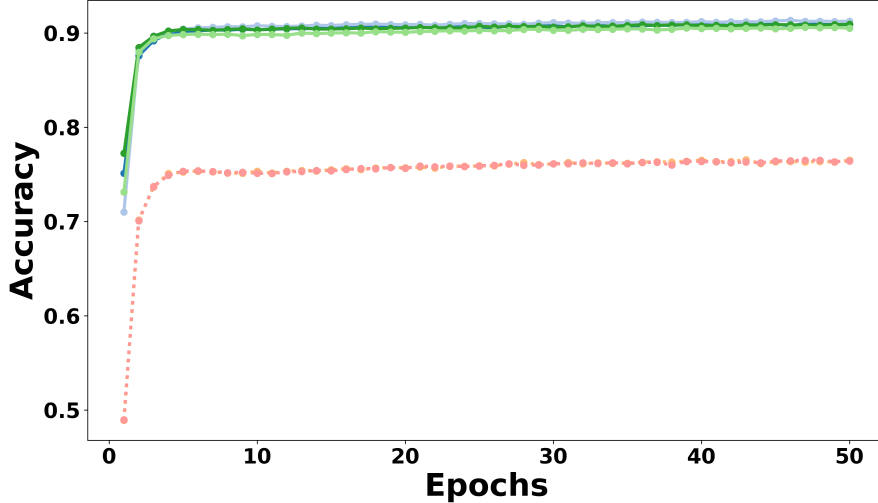
| Dataset | Arch. | T | Accuracy | F1-score | Time/Epoch (s) |
|----------|-------|-----|----------|----------|----------------|
| CIFAR-10 | 1SADP | 25 | 0.7061 | 0.6922 | 18.88 |
| CIFAR-10 | 1SADP | 100 | 0.7069 | 0.6974 | 31.79 |
| CIFAR-10 | 2SADP | 25 | 0.6850 | 0.6601 | 18.70 |
| CIFAR-10 | 2SADP | 100 | 0.6927 | 0.6711 | 18.64 |
| FMNIST | 1SADP | 25 | 0.8969 | 0.8955 | 22.36 |
| FMNIST | 1SADP | 100 | 0.8853 | 0.8776 | 22.72 |
| FMNIST | 2SADP | 25 | 0.8991 | 0.8969 | 22.28 |
| FMNIST | 2SADP | 100 | 0.8995 | 0.8955 | 22.26 |
| MNIST | 1SADP | 25 | 0.9909 | 0.9909 | 49.24 |
| MNIST | 1SADP | 100 | 0.9916 | 0.9915 | 22.48 |
| MNIST | 2SADP | 25 | 0.9893 | 0.9896 | 22.89 |
| MNIST | 2SADP | 100 | 0.9915 | 0.9915 | 22.22 |

low-complexity grayscale images, achieved reasonable performance, with evaluation accuracies of 0.75 and 0.87, respectively. However, CIFAR-10, being a color dataset with complex textures and object boundaries, showed poor performance (around 0.23) in 1SADP with timestep 25. The purely brightness-based Poisson encoding fails to capture high-level spatial and chromatic correlations, leading to weak feature separability in such visually complex datasets.

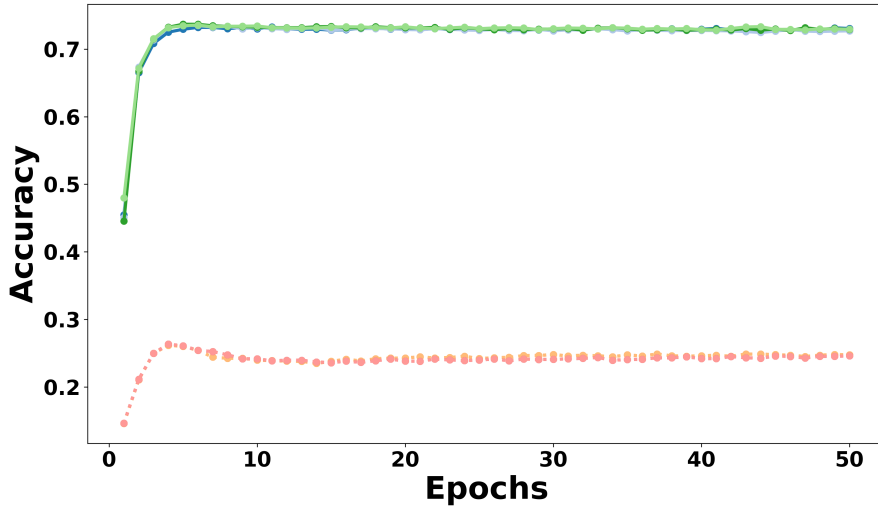
To address this limitation, a CNN+Poisson hybrid encoding strategy was introduced. In this scheme, a CNN first extracts essential spatial and color-invariant features, which are then converted into spike trains using the Poisson process. As summarized in Table 3, this combination led to significant performance improvements across all datasets. For CIFAR-10, evaluation accuracy increased from 0.23 to 0.70, and the F1-score improved from 0.17 to 0.69, confirming that CNN preprocessing effectively highlights critical feature maps for spike-based learning. For grayscale datasets such as MNIST and FMNIST, CNN+Poisson further enhanced accuracy to 0.99 and 0.88, respectively, indicating refined feature extraction and reduced noise in spike generation.

Noticeably, the results are absolutely **at-par with the state-of-the-art** (see Table 1) for local learning models as reported in a recent work by Tian *et al.* [48].

Comparison of 1SADP and 2SADP Architectures The 1SADP and 2SADP architectures exhibited similar overall performance, with only marginal differences in evaluation metrics. There is no solid evidence that adding a deep layer to the existing architecture improves learning. For Poisson-only encoding only a slight improvement is observed for 2SADP over the 1SADP model



(a) FMNIST



(b) CIFAR10

..... 1SADP | Poisson_Only | T=25 2SADP | Poisson_Only | T=25 — 1SADP | CNN+Poisson | T=25 — 2SADP | CNN+Poisson | T=25
 1SADP | Poisson_Only | T=100 2SADP | Poisson_Only | T=100 — 1SADP | CNN+Poisson | T=100 — 2SADP | CNN+Poisson | T=100

Figure 2: Validation accuracy for FMNIST and CIFAR10. Note the large difference of accuracy between Poisson encoding and CNN+Poisson encoding for CIFAR10 dataset. CIFAR10 is a more complex dataset and the classification relies on not just pixel-brightness-based features.

for the MNIST and FMNIST datasets. For CNN+Poisson encoding a similar slight improvement is observed for the FMNIST dataset only.

Impact of Timestep Variations Increasing the number of timesteps from 25 to 100 yielded moderate gains for simpler datasets such as MNIST, where longer temporal windows allow finer encoding of spike dynamics. For none of the datasets any exceptional gain in Accuracy and F1-score was noticed. Even for runtime, no significant difference was noticed, probably because the number of timesteps is never too high.

Computational Efficiency The CNN+Poisson encoder not only achieved higher accuracy but also significantly reduced training time per epoch. This is obvious because the CNN extracts 256 features which is much lesser than the original feature dimension which is used for the Poisson-only case. The MNIST model using Poisson-only encoding required approximately 55 seconds per epoch, while the CNN+Poisson configuration completed training in about 32 seconds per epoch. This efficiency arises from the CNN’s dimensionality reduction and selective feature extraction, which lower spike event density and computational load. Hence, the hybrid encoder balances representational richness with computational efficiency.

Positioning with respect to existing SNN benchmarks. Table 1 summarizes representative results from recent SNN benchmarks reported by Tian et al. [48]. We emphasize that our goal is not to outperform gradient-based SNNs, but to demonstrate that strictly local learning can reach competitive performance. These results show that classical pairwise STDP achieves accuracies of approximately 85.3% on Fashion-MNIST and fails to scale to CIFAR-10, while more advanced synchrony-based rules such as S2-STDP and NCG-S2-STDP improve performance to 85.9% on Fashion-MNIST and up to 66.4% on CIFAR-10 when convolutional structures are employed. Despite these improvements, performance on CIFAR-10 remains substantially lower than that achieved by gradient-based or hybrid learning methods.

In comparison, the proposed Supervised SADP framework achieves competitive or superior performance while retaining strictly local, gradient-free learning. Using CNN+Poisson encoding, supervised SADP attains accuracies of 99.1% on MNIST, 89.9% on Fashion-MNIST, and approximately 70.7% on CIFAR-10 (Table 3). Notably, the CIFAR-10 accuracy exceeds the best synchrony-based SNN results reported in Table 1 (e.g., 66.4% for NCG-S2-STDP), despite employing a simpler feed-forward spiking architecture without recurrent dynamics or error backpropagation.

Another fact that **we want to emphasize on** is, beyond accuracy, supervised SADP demonstrates substantial gains in computational efficiency. For CIFAR-10, CNN+Poisson configurations train in approximately 18–32 seconds per epoch, compared to Poisson-only SNN configurations requiring over 230 seconds per epoch and many prior STDP-based approaches reporting similarly high computational overhead. These speedups arise from linear-time agreement-based updates and reduced spike dimensionality following convolutional preprocessing. Classical local learning using STDP is extremely slow when run in standard system with 64 GB RAM. As reported in *Bej et al.* per epoch runtime is around 30 minutes for MNIST and FMNIST datasets [2]. In contrast, the Poisson encoding version of Supervised SADP takes less than four minutes per epoch on an average with comparable computation resources. Together, these results indicate that supervised SADP offers a favorable accuracy–efficiency trade-off relative to existing SNN benchmarks, particularly for visually complex datasets.

5.2 Results on Biomedical Image Classification

Overall performance trends. Table 4 summarizes the performance of SADP-based models across three biomedical imaging datasets under varying architectural depth, encoding strategies, and temporal resolutions. Across all datasets and timesteps, configurations employing CNN+Poisson encoding consistently outperform their Poisson-only counterparts in terms of both classification accuracy and macro F1-score. These results highlight the importance of structured feature representations for effective spike-based learning in complex biomedical imaging tasks.

Colon histopathology. On the Colon Histopathology dataset, models using Poisson-only encoding achieve moderate performance, with accuracies ranging between 0.63 and 0.66 across architectures and timesteps. Introducing convolutional preprocessing leads to substantial performance gains. In particular, the 1SADP model achieves an accuracy of 0.9135 at $T = 100$, while the 2SADP configuration reaches near-perfect performance, achieving both accuracy and F1-score of 0.9985. These results indicate that convolutional feature extraction effectively captures discriminative tissue morphology and color patterns that are otherwise inaccessible to brightness-driven spike encoding.

Lung histopathology. A similar trend is observed for the Lung Histopathology dataset. While Poisson-only models achieve accuracies in the range of 0.73–0.74, CNN+Poisson configurations consistently attain accuracies between 0.96 and 0.98, accompanied by strong improvements in F1-

score. Notably, these gains are obtained with low computational overhead, with the average training time per epoch remaining below six seconds for all CNN+Poisson variants, demonstrating the efficiency of the proposed hybrid CNN-SNN pipeline.

Brain tumor MRI. The Brain Tumor MRI dataset presents a grayscale imaging scenario with reduced chromatic variability. In this setting, Poisson-only models achieve stable accuracies of approximately 0.86 but exhibit low F1-scores around 0.46, indicating poor class separability. Incorporating convolutional preprocessing significantly improves both accuracy and class discrimination, with CNN+Poisson configurations achieving accuracies up to 0.99 and F1-scores approaching 0.98. These results demonstrate that spatial feature abstraction remains critical for effective spike agreement even in grayscale domains.

Table 4: Performance Summary of SADP-based Models on Bio-Inspired Datasets

| Dataset | Architecture | Timestep | Encoding | Accuracy | F1-score | Avg Time/Epoch (s) |
|-------------------------------------|--------------|--------------|----------|----------|----------|--------------------|
| Colon Histopathology (Color) | | | | | | |
| 1SADP | 25 | Poisson-only | 0.6600 | 0.6595 | 29.34 | |
| 1SADP | 100 | Poisson-only | 0.6600 | 0.6595 | 45.84 | |
| 2SADP | 25 | Poisson-only | 0.6355 | 0.6232 | 31.40 | |
| 2SADP | 100 | Poisson-only | 0.6355 | 0.6232 | 30.36 | |
| 1SADP | 25 | CNN+Poisson | 0.9085 | 0.9079 | 6.12 | |
| 1SADP | 100 | CNN+Poisson | 0.9135 | 0.9164 | 3.90 | |
| 2SADP | 25 | CNN+Poisson | 0.8690 | 0.8666 | 8.43 | |
| 2SADP | 100 | CNN+Poisson | 0.9985 | 0.9985 | 3.95 | |
| Lung Histopathology (Color) | | | | | | |
| 1SADP | 25 | Poisson-only | 0.7300 | 0.7266 | 60.61 | |
| 1SADP | 100 | Poisson-only | 0.7300 | 0.7266 | 56.95 | |
| 2SADP | 25 | Poisson-only | 0.7380 | 0.7287 | 56.67 | |
| 2SADP | 100 | Poisson-only | 0.7380 | 0.7287 | 43.40 | |
| 1SADP | 25 | CNN+Poisson | 0.9650 | 0.9649 | 5.99 | |
| 1SADP | 100 | CNN+Poisson | 0.9656 | 0.9637 | 5.96 | |
| 2SADP | 25 | CNN+Poisson | 0.9706 | 0.9701 | 5.93 | |
| 2SADP | 100 | CNN+Poisson | 0.9843 | 0.9843 | 6.09 | |
| Brain Tumor MRI (Grayscale) | | | | | | |
| 1SADP | 25 | Poisson-only | 0.8586 | 0.4620 | 63.27 | |
| 1SADP | 100 | Poisson-only | 0.8586 | 0.4620 | 71.29 | |
| 2SADP | 25 | Poisson-only | 0.8586 | 0.4620 | 71.54 | |
| 2SADP | 100 | Poisson-only | 0.8586 | 0.4620 | 63.53 | |
| 1SADP | 25 | CNN+Poisson | 0.9845 | 0.9688 | 8.46 | |
| 1SADP | 100 | CNN+Poisson | 0.9887 | 0.9790 | 8.48 | |
| 2SADP | 25 | CNN+Poisson | 0.9827 | 0.9654 | 8.44 | |
| 2SADP | 100 | CNN+Poisson | 0.9723 | 0.9487 | 16.02 | |

Interpretation and implications. The results on biomedical datasets demonstrate the robustness and adaptability of the proposed Supervised SADP framework across diverse imaging modalities. In color histopathological datasets, performance improvements obtained through CNN+Poisson encoding highlight the importance of rich texture and color information for effective spike-based learning. Brightness-driven Poisson encoding alone fails to capture the complex spatial and chromatic patterns characteristic of tissue morphology, resulting in limited discriminative power.

The integration of convolutional feature extraction prior to spike generation enables the spiking network to receive structured, semantically meaningful spike patterns. SADP then exploits these patterns through agreement-driven plasticity, reinforcing neuron assemblies that consistently align with diagnostic output activity. The near-perfect performance observed in colon and lung histopathology tasks underscores the strong synergy between convolutional preprocessing and local spike-based learning.

In contrast, the Brain Tumor MRI dataset presents a grayscale setting with reduced chromatic variability. While Poisson-only encoding achieves reasonable accuracy, its low F1-score indicates insufficient class discrimination. The marked improvement obtained through convolutional preprocessing demonstrates that even in grayscale domains, spatial feature abstraction is critical for effective spike

agreement. These results confirm that SADP remains effective when provided with enriched feature representations.

The consistent trends observed across biomedical, standard vision, and neuromorphic benchmarks validate the generalization capability of the proposed learning mechanism. The hybrid CNN-SNN architecture preserves strictly local learning within the spiking network while leveraging convolutional encoders as sensory front-ends, enabling SADP to scale to complex real-world visual tasks without sacrificing biological plausibility.

5.3 Additional Experiments

Hyperparameter Sensitivity and Robustness. To assess the robustness of the proposed Supervised SADP framework and to ensure that the reported performance does not rely on aggressive or dataset-specific tuning, we performed a systematic hyperparameter sensitivity analysis using Bayesian optimization (Optuna). The study indicates that learning dynamics are primarily influenced by the learning rate decay and the output-layer learning rate, both of which control the stability and convergence speed of supervised Hebbian updates. In contrast, parameters such as membrane thresholds, number of timesteps, and input learning rates exhibit relatively low sensitivity within reasonable operating ranges. This behavior suggests that Supervised SADP maintains stable learning across a broad parameter regime and does not require fine-grained calibration to achieve competitive performance. Detailed optimization trajectories and parameter importance analyses are provided in Appendix A.

Device-Inspired Plasticity and Hardware Compatibility. In addition to algorithmic evaluation, we examined the compatibility of Supervised SADP with experimentally measured synaptic update dynamics derived from iontronic memtransistor devices following the work of Bej *et al.* [2]. Specifically, potentiation and depression trajectories extracted from hardware measurements were fitted using smooth spline interpolation and directly integrated into the SADP learning rule. These device-inspired kernels yield slightly lower accuracy compared to idealized update functions. Importantly, SADP does not assume symmetric, continuous, or perfectly linear weight updates, allowing it to operate under non-ideal and asymmetric device constraints. This analysis, detailed in Appendix B, should be viewed as a demonstration of algorithmic compatibility with emerging neuromorphic substrates rather than a full hardware deployment.

Limitations and open challenges. While the proposed Supervised SADP framework demonstrates strong empirical performance and favorable efficiency–accuracy trade-offs, several limitations warrant discussion.

First, although the two-hidden-layer 2SADP architecture exhibits stable learning and occasionally improved regularization behavior, its performance gains over 1SADP remain modest and dataset-dependent. This suggests that, in its current feedforward form, deeper SADP architectures do not yet provide a clear or consistent advantage, likely due to the absence of explicit mechanisms for hierarchical credit assignment or inter-layer coordination beyond local spike agreement. Understanding when and how agreement-based plasticity benefits from additional depth remains an open question.

Second, the reliance on a pretrained convolutional encoder in the CNN+Poisson configuration introduces a hybrid learning pipeline in which only the spiking component is trained using local plasticity. While this design preserves strict locality within the SNN and significantly improves performance on complex visual data, the convolutional front-end itself is not learned in a spike-driven or fully local manner. Consequently, end-to-end on-chip deployment would require either pretraining the CNN off-chip, mapping it to neuromorphic hardware, or replacing it with a spiking-compatible feature extractor. Developing fully spike-native or co-trained sensory front-ends remains an important direction for future work.

Third, although supervised SADP avoids backpropagation, surrogate gradients, and teacher forcing, it currently operates in a feedforward setting with static inputs and image-level classification tasks. Extensions to temporally structured inputs, recurrent architectures, and sequence learning may require additional stabilization mechanisms or modified agreement metrics to prevent spurious synchronization or vanishing agreement signals. Finally, while device-inspired synaptic kernels demonstrate compatibility with non-ideal hardware dynamics, current results indicate a mild per-

formance gap relative to idealized update functions, underscoring the need for improved device calibration and variability-aware learning rules.

Together, these limitations highlight that Supervised SADP should be viewed not as a replacement for deep gradient-based learning, but as a complementary, biologically grounded alternative that offers strong locality, efficiency, and hardware alignment, while leaving several important architectural and deployment challenges open for future investigation.

Key takeaways.

- **Fast supervised local learning without backpropagation.** Supervised SADP demonstrates that effective supervised learning in spiking neural networks can be achieved using strictly local, spike-driven plasticity rules. By replacing spike-pair timing with agreement-based statistics, the proposed method enables linear-time synaptic updates, fast convergence, and competitive accuracy without relying on backpropagation, surrogate gradients, reward modulation, or teacher forcing. This establishes agreement-driven plasticity as a viable and scalable alternative for supervised SNN training.
- **A principled sensory front-end for scalable spike-based learning.** The integration of a CNN-based feature extractor as a frozen sensory front-end provides a principled solution for extending local spike-based learning to visually complex data. Convolutional preprocessing transforms raw sensory inputs into structured, semantically meaningful representations, which are then converted into spike trains suitable for agreement-driven plasticity. More broadly, these results highlight a necessary paradigm shift in spike-based learning: complex perceptual tasks cannot be addressed by relying solely on brightness-driven or naïve spike generation schemes. Expecting a spiking network to discover rich semantic structure from unstructured intensity-based spike trains places an unrealistic burden on local synaptic plasticity alone. By decoupling sensory representation from spike-based learning, the proposed hybrid design preserves strict locality within the spiking network while enabling SADP to scale from simple grayscale datasets to color natural images and biomedical modalities, offering a practical pathway toward deployable hybrid CNN–SNN systems.

6 Conclusion

We presented a supervised extension of Spike Agreement–Dependent Plasticity (SADP), termed Supervised SADP learning, that enables efficient and biologically grounded supervised learning in spiking neural networks (SNNs). By replacing precise spike-pair timing with statistical agreement measures such as Cohen’s κ , the proposed learning rule generalizes classical STDP while retaining strict locality, linear-time complexity, and hardware-friendly implementation.

Extensive evaluations on benchmark vision datasets (MNIST, Fashion-MNIST, and CIFAR-10) and biomedical imaging tasks demonstrate that supervised SADP achieves robust classification performance without relying on backpropagation, surrogate gradients, or teacher forcing. When combined with a lightweight convolutional front-end, the framework scales effectively to complex visual domains while preserving local spike-driven learning within the SNN. The results highlight a favorable trade-off between biological plausibility, computational efficiency, and practical performance.

Importantly, the proposed learning mechanism is compatible with device-inspired synaptic update dynamics, as demonstrated through spline-based kernels derived from iontronic memtransistor measurements. While this study focuses on feedforward architectures and image classification tasks, the results establish supervised SADP as a promising foundation for scalable, interpretable, and hardware-aligned learning in spiking neural systems. Future work will explore extensions to deeper architectures and temporally structured tasks.

All of our results are reproducible using the codes available in our [GitHub repository](#).

References

- [1] Logan A. Becker, François Baccelli, and Thibaud Taillefumier. Subthreshold variability of neuronal populations driven by synchronous synaptic inputs, 2025. Preprint.

- [2] Saptarshi Bej, Muhammed E. Sahad, Gouri Lakshmi, Harshit Kumar, Pritam Kar, and Bikas C. Das. Spike agreement dependent plasticity: A scalable bio-inspired learning paradigm for spiking neural networks, 2025.
- [3] Guo-qiang Bi and Mu-ming Poo. Synaptic modifications in cultured hippocampal neurons: dependence on spike timing, synaptic strength, and postsynaptic cell type. *Journal of neuroscience*, 18(24):10464–10472, 1998.
- [4] Guo-Qiang Bi and Mu-Ming Poo. Synaptic modification by correlated activity: Hebb’s postulate revisited. *Annual review of neuroscience*, 24(1):139–166, 2001.
- [5] Elie L Bienenstock, Leon N Cooper, and Paul W Munro. Theory for the development of neuron selectivity: orientation specificity and binocular interaction in visual cortex. *Journal of Neuroscience*, 2(1):32–48, 1982.
- [6] Johannes Bill and Robert Legenstein. A compound memristive synapse model for statistical learning through stdp in spiking neural networks. *Frontiers in Neuroscience*, 8:412, 2014.
- [7] Andrew A. Borkowski, Marilyn M. Bui, L. Brannon Thomas, Catherine P. Wilson, Lauren A. DeLand, and Stephen M. Mastorides. Lc25000 lung and colon histopathological image dataset.
- [8] D. Chawla, E. D. Lumer, and K. J. Friston. The relationship between synchronization among neuronal populations and their mean activity levels. *Neural Computation*, 11(6):1389–1411, 1999.
- [9] Claudia Clopath, Lars Büsing, Eleni Vasilaki, and Wulfram Gerstner. Connectivity reflects coding: a model of voltage-based stdp with homeostasis. *Nature neuroscience*, 13(3):344–352, 2010.
- [10] Claudia Clopath and Wulfram Gerstner. Voltage and spike timing interact in stdp – a unified model. *Frontiers in Synaptic Neuroscience*, 2:25, 2010.
- [11] Gregory K. Cohen, Garrick Orchard, Sio-Hoi Leng, Jonathan Tapson, Ryad B. Benosman, and André Van Schaik. Skimming digits: Neuromorphic classification of spike-encoded images. *Frontiers in Neuroscience*, 10:184, 2016.
- [12] Mike Davies, Narayan Srinivasa, Tian-Ming Lin, Ganesh Chinya, Yong Cao, Sriharsha Choday, George Deal, Panos Dimoulas, Brian Felt, Andreas Fiebig, et al. Loihi: A neuromorphic manycore processor with on-chip learning. *IEEE Micro*, 38(1):82–99, 2018.
- [13] Peter U Diehl and Matthew Cook. Unsupervised learning of digit recognition using spike-timing-dependent plasticity. *Frontiers in Computational Neuroscience*, 9:99, 2015.
- [14] Meng Dong, Xuhui Huang, and Bo Xu. Unsupervised speech recognition through spike-timing-dependent plasticity in a convolutional spiking neural network. *PLoS ONE*, 13(11):e0204596, 2018.
- [15] Paul Ferré, Franck Mamalet, and Simon J. Thorpe. Unsupervised feature learning with winner-takes-all based stdp. *Frontiers in Computational Neuroscience*, 12:24, 2018.
- [16] Alexandre Foncelle, Alexandre Mendes, et al. Modulation of spike-timing dependent plasticity: Towards the inclusion of a third factor in computational models. *Frontiers in Computational Neuroscience*, 12:49, 2018.
- [17] Nicolas Frémaux and Wulfram Gerstner. Neuromodulated spike-timing-dependent plasticity, and theory of three-factor learning rules. *Frontiers in Neural Circuits*, 9:85, 2016.
- [18] Wulfram Gerstner, Werner M. Kistler, Richard Naud, and Liam Paninski. *Neuronal Dynamics: From Single Neurons to Networks and Models of Cognition*. Cambridge University Press, 2014.
- [19] Gaspard Goupy, Pierre Tirilly, and Ioan Marius Bilasco. Neuronal competition groups with supervised stdp for spike-based classification, 2024.
- [20] Stefan Habenschuss, Helmut Pühr, and Wolfgang Maass. Emergence of optimal decoding of population codes through stdp. *Neural Computation*, 25(6):1371–1407, 2013.

[21] Yunzhe Hao, Xuhui Huang, Meng Dong, and Bo Xu. A biologically plausible supervised learning method for spiking neural networks using the symmetric stdp rule. *Neural Networks*, 121:387–395, 2020.

[22] Harel Hazan, Daniel J Saunders, Hina Khan, Dhruvil Patel, Dhaval T Sanghavi, Hava T Siegelmann, and Robert Kozma. Bindsnet: A machine learning-oriented spiking neural networks library in python. *Frontiers in Neuroinformatics*, 12:89, 2018.

[23] D. O. Hebb. *The Organization of Behavior*. Wiley, 1949.

[24] Eugene M. Izhikevich. Solving the distal reward problem through linkage of stdp and dopamine signaling. *Cerebral Cortex*, 17(10):2443–2452, 2007.

[25] Saeed R. Kheradpisheh, Mohammad Ganjtabesh, and Timothée Masquelier. Bio-inspired unsupervised learning of visual features leads to robust invariant object recognition. *Neurocomputing*, 205:382–392, 2016.

[26] Saeed R. Kheradpisheh, Mohammad Ganjtabesh, Simon J. Thorpe, and Timothée Masquelier. Stdःp-based spiking deep convolutional neural networks for object recognition. *Neural Networks*, 99:56–67, 2018.

[27] Harold J. Kushner and G. George Yin. *Stochastic Approximation and Recursive Algorithms and Applications*. Applications of Mathematics. Springer, 2nd edition, 2003.

[28] Hyun Jun Lee, Ju Hyun Hwang, Kyung Bok Choi, Sun-Gyu Jung, Kyu Nyun Kim, Yong Sub Shim, Cheol Hwee Park, Young Wook Park, and Byeong-Kwon Ju. Effective indium-doped zinc oxide buffer layer on silver nanowires for electrically highly stable, flexible, transparent, and conductive composite electrodes. *ACS Applied Materials & Interfaces*, 5(21):10397–10403, 2013.

[29] Ralph Linsker. From basic network principles to neural architecture: Emergence of orientation columns. *Proceedings of the National Academy of Sciences*, 83(21):8779–8783, 1986.

[30] Henry Markram, Wulfram Gerstner, and Per Jesper Sjöström. A history of spike-timing-dependent plasticity. *Frontiers in Synaptic Neuroscience*, 3:4, 2011.

[31] Henry Markram, Wulfram Gerstner, and Per Jesper Sjöström. Spike-timing-dependent plasticity: A comprehensive overview. *Frontiers in Synaptic Neuroscience*, 4:2, 2012.

[32] Henry Markram, Joachim Lübke, Michael Frotscher, and Bert Sakmann. Regulation of synaptic efficacy by coincidence of postsynaptic aps and epsps. *Science*, 275(5297):213–215, 1997.

[33] Timothée Masquelier, Rudy Guyonneau, and Simon J. Thorpe. Spike timing dependent plasticity finds the start of repeating patterns in continuous spike trains. *PLoS ONE*, 3(1):e1377, 2008.

[34] Timothée Masquelier and Simon J. Thorpe. Unsupervised learning of visual features through spike timing dependent plasticity. *PLoS Computational Biology*, 3(2):e31, 2007.

[35] Kenneth D. Miller and David J.C. MacKay. The role of constraints in hebbian learning. *Neural Computation*, 6(1):100–126, 1994.

[36] Abigail Morrison, Markus Diesmann, and Wulfram Gerstner. Phenomenological models of synaptic plasticity based on spike timing. *Biological Cybernetics*, 98(6):459–478, 2008.

[37] A. Mukherjee et al. Superionic rubidium silver iodide gated low voltage synaptic transistor. *Applied Physics Letters*, 119(25):253502, 2021.

[38] Bernhard Nessler, Michael Pfeiffer, Lars Buesing, and Wolfgang Maass. Bayesian computation emerges in generic cortical microcircuits through spike-timing-dependent plasticity. *PLoS Computational Biology*, 9(4):e1003037, 2013.

[39] Msoud Nickparvar. Brain tumor mri dataset, 2021.

[40] Erkki Oja. A simplified neuron model as a principal component analyzer. *Journal of mathematical biology*, 15(3):267–273, 1982.

[41] Jean-Pascal Pfister and Wulfram Gerstner. Triplets of spikes in a model of spike timing-dependent plasticity. *Journal of Neuroscience*, 26(38):9673–9682, 2006.

[42] S. Sagar, A. Dey, and B. C. Das. Unconventional redox-active gate dielectrics to fabricate high performance organic thin-film transistors. *ACS Applied Electronic Materials*, 1(11):2314–2324, 2019.

[43] S. Sagar, K. Udaya Mohanan, S. Cho, et al. Emulation of synaptic functions with low voltage organic memtransistor for hardware oriented neuromorphic computing. *Scientific Reports*, 12(1):3808, 2022.

[44] Vahid Saranirad, Shirin Dora, Thomas Martin McGinnity, and Damien Coyle. CDNA-SNN: A new spiking neural network for pattern classification using neuronal assemblies. *IEEE Transactions on Neural Networks and Learning Systems*, 2024.

[45] Per Jesper Sjöström, Gina G Turrigiano, and Sacha B Nelson. Rate, timing, and cooperativity jointly determine cortical synaptic plasticity. *Neuron*, 32(6):1149–1164, 2001.

[46] Sen Song, Kenneth D Miller, and L F Abbott. Competitive hebbian learning through spike-timing-dependent synaptic plasticity. *Nature Neuroscience*, 3(9):919–926, 2000.

[47] Marcel Stimberg, Romain Brette, and Dan FM Goodman. Brian 2, an intuitive and efficient neural simulator. *eLife*, 8:e47314, 2019.

[48] Yuchen Tian, Assel Kembay, Nhan Duy Truong, Jason K. Eshraghian, and Omid Kavehei. Beyond pairwise plasticity: Group-level spike synchrony facilitates efficient learning in spiking neural networks, 2025. Preprint.

[49] Yoeri van de Burgt, Armantas Melianas, Scott T. Keene, et al. Organic electronics for neuromorphic computing. *Nature Electronics*, 1(7):386–397, 2018.

[50] X. Yang and B. Doiron. Causal spike timing dependent plasticity prevents assembly fusion in recurrent networks, 2025.

[51] Dongcheng Zhao, Yi Zeng, Tielin Zhang, Mengting Shi, and Feifei Zhao. GLSNN: A multi-layer spiking neural network based on global feedback alignment and local stdp plasticity. *Frontiers in Computational Neuroscience*, 14:576841, 2020.

Appendix A: Hyperparameter Optimization using Optuna

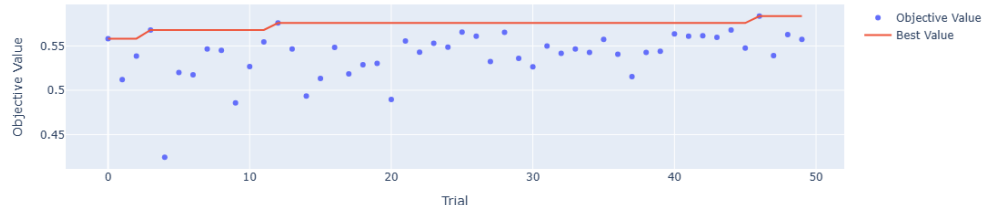


Figure 3: Optimization history plot showing the evolution of validation accuracy across 50 Optuna trials. Blue dots indicate individual trial accuracies, while the orange line represents the cumulative best value. Significant improvements occur around Trials 4, 12–14, and 46–48, reaching a best accuracy of approximately 0.57.

Hyperparameter sensitivity analysis was performed using Optuna, a Bayesian optimization framework built on the Tree-structured Parzen Estimator (TPE). The analysis targeted the CNN+Poisson encoding configuration of the spiking neural network (SNN), with each trial trained for 10 epochs to

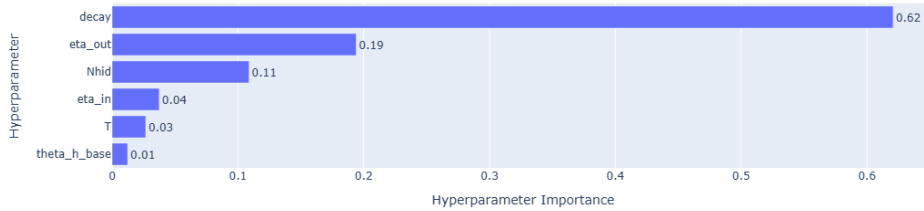


Figure 4: Hyperparameter importance plot illustrating the relative contribution of each parameter to model performance. Learning rate decay dominates with an importance of 0.62, followed by output learning rate (η_{out}) and hidden layer size (N_{hid}).

ensure a balance between convergence stability and computational feasibility. Six key hyperparameters were tuned: hidden layer size (N_{hid} , 100–500), membrane threshold base (θ_h , 0.3–0.7), output learning rate (η_{out} , 10^{-5} – 10^{-3} , log-uniform), input learning rate (η_{in} , 10^{-5} – 10^{-3} , log-uniform), learning rate decay (0.995–0.9999), and number of timesteps (T , 10–50).

A total of 50 optimization trials were conducted, and Optuna’s asynchronous median pruning strategy was applied to terminate underperforming trials early, thereby improving the search efficiency.

The optimization history plot Figure 3 revealed the progression of the objective function (validation accuracy) across trials. Each blue point represented the accuracy achieved in a single trial, while the orange line denoted the cumulative best performance. The objective values ranged approximately from 0.42 to 0.57, with a clear upward trend indicating successful optimization. Significant improvements were observed around Trials 4, 12–14, and 46–48, suggesting that the optimizer progressively explored and exploited more promising hyperparameter regions. The plateau between Trials 15 and 45 reflected a phase of convergence before a final improvement near the end, where the best validation accuracy of approximately 0.57 was achieved.

The hyperparameter importance plot Figure 4 quantified the relative influence of each parameter on model performance. The learning rate decay emerged as the most dominant factor, contributing 62% of the total importance, indicating that fine-tuning decay plays a critical role in achieving stable weight adaptation in SNNs. The output learning rate (η_{out}) and hidden layer size (N_{hid}) followed with importances of 19% and 11%, respectively, suggesting that both network capacity and gradient scaling significantly affect convergence. In contrast, parameters such as input learning rate (η_{in}), number of timesteps (T), and membrane threshold base (θ_h) had relatively minor effects (<5%), implying reduced sensitivity within the explored ranges.

Together, these diagnostic analyses demonstrate that while Optuna efficiently identified promising hyperparameter regions, the SNN’s performance was particularly sensitive to decay-related adjustments and output learning rate tuning. The study thus served as a hyperparameter sensitivity investigation rather than an exhaustive search for a single optimal configuration, providing valuable insights into which parameters most strongly shape SNN learning dynamics.

Appendix B: Device-Based Evaluation of Weight Update Mechanisms

To enable hardware realism, we extracted potentiation and depression trajectories from iontronic memtransistors and incorporated them into the SADP update kernels, following the work of Bej *et al.* [2]. The experimentally measured conductance changes were fitted using smooth spline interpolation, producing bounded and continuous device-specific weight-update functions like in figure 5.

These spline-based kernels were directly integrated into the Supervised-Spike-Agreement–Dependent Plasticity (SADP) framework, allowing the learning dynamics in simulation to closely follow the physical device behavior. This should be viewed as device-inspired validation rather than a full hardware deployment: the goal is to demonstrate that Supervised-SADP is inherently compatible with emerging memtransistor technologies. Importantly, SADP is not restricted to idealized or hand-crafted update curves—its local and fast weight updates allow it to learn

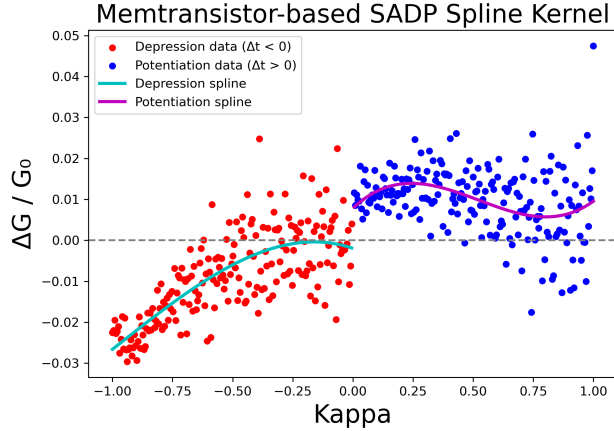


Figure 5: Device-inspired SADP.

Table 5: Performance Comparison Across Datasets and Timesteps

| Dataset | Timestep | Accuracy | F1-score | Avg Time/Epoch (s) |
|---------|----------|----------|----------|--------------------|
| MNIST | 25 | 0.8238 | 0.8192 | 206.80 |
| MNIST | 100 | 0.8238 | 0.8192 | 207.07 |
| FMNIST | 25 | 0.7025 | 0.6721 | 226.28 |
| FMNIST | 100 | 0.7025 | 0.6721 | 207.44 |

directly from hardware-measured kernels. While current device-derived kernels yield slightly lower performance than the ideal spline baseline, their effectiveness improves as the device response more closely approximates the ideal form. This establishes a clear pathway for hardware integration, where advances in device calibration and fabrication can translate directly into better learning performance. For completeness, we evaluated device-specific SADP kernels on the MNIST and FMNIST datasets using Poisson encoding under two temporal resolutions (25 and 100 timesteps).